Supplementary Materials

Molecular engineering of g-C$_3$N$_4$ with spatial charge separation for enhancing photocatalytic performances

Mingrui Guo[a,b], Meng Chen[a,b], Jixiang Xu[a, b,]*, Jing Wang[b], Lei Wang[a,c,]*

[a]*Key Laboratory of Eco-chemical Engineering, Taishan Scholar Advantage and Characteristic Discipline Team of Eco-Chemical Process and Technology, Qingdao University of Science and Technology, Qingdao 266042, China*

[b]*College of Chemistry and Molecular Engineering, Qingdao University of Science and Technology, Qingdao 266042, China*

[c]*College of Environment and Safety Engineering, Qingdao University of Science and Technology, Qingdao, Shandong 266042, China*

* Corresponding Authors: xujix47@163.com (J.X. Xu); inorchemwl@126.com (L. Wang)

Experimental section

Characterization

Powder X-ray diffraction (XRD) data were obtained using a Rigaku D-MAX 2500/PC diffractometer. Fourier transform infrared (FTIR) spectra were recorded on a Nicolet 6700 spectrometer with KBr pellet (Thermo scientific, USA). X-ray photoelectron spectra (XPS) were recorded using an X-ray photoelectron spectrometer (Thermo Scientific, Kα) equipped with a monochromatic Al Kα X-ray source (hv = 1486.6 eV). UV–visible diffuse reflectance spectra were recorded using a Lambda 750 UV/VIS/NIR spectrometer. The morphology of samples was observed using a JEOL 7600F scanning electron microscope (SEM). High-resolution transmission electron microscopy (HRTEM) images and energy-dispersive X-ray spectroscopy (EDS) elemental mapping were obtained using a Tecnai-G^2-F30 high-resolution transmission electron microscope (FEI Company, USA). Photoluminescence (PL) spectra with an excitation wavelength of 529 nm were recorded using a fluorescence spectrophotometer (F-4500 FL). The specific surface area and pore structure were confirmed via Brunauer-Emmett-Teller (BET) method and Barrett-Joyner-Halenda (BJH) on ASAP 2460. The electron spin resonance (EPR) experiments were performed by using the Bruker E500 instrument to detect the carbon vacancy. The solid-state ^{13}C nuclear magnetic resonance (NMR) spectra were measured on the Agilent-NMR-vnmrs 600 instrument.

Calculation of the apparent quantum yield (AQY)

The AQY was calculated using the following equation:

$$AQY = \frac{Number\ of\ reacted\ electrons}{Number\ of\ incident\ photons} \times 100\%$$

$$= \frac{2 \times number\ of\ evolved\ H_2\ molecules}{Number\ of\ incident\ photons} \times 100\%$$

$$= \frac{2 \times n_{H_2}}{n_p} \times 100\%$$

$$= \frac{2 \times n_{H_2}}{\dfrac{P \times t \times \lambda}{h \times c}} \times 100\%$$

In this equation, n_{H_2} and n_p is the number of H_2 molecules and photons, respectively, P denotes the light power, determined by CEL-NP2000 power meter; t is the illumination time (3600 s); λ is the incident light wavelength (420 nm); h represents the Planck constant (6.63×10^{-34} J·s); and c is the light speed (3.0×10^8 m·s^{-1}).

Electrochemical and photoelectrochemical measurements

The photocurrent measurements, linear sweep voltammetry (LSV), and electrochemical impedance spectroscopy (EIS) were recorded using a standard three-electrode electrochemical analyzer (PEC2000, Beijing). The as-prepared sample coated onto an FTO electrode acts as the working electrode; a SCE (saturated calomel electrode) acts as the reference electrode; a Pt foil acts as the counter electrode. A 300-W Xe arc lamp (PLS-SXE300) was used as the light source. A 0.5 M Na_2SO_4 aqueous solution was used as the electrolyte.

Calculation methods

Gaussian 09 program was employed for DFT calculations. Ground state geometry optimization was performed at B3LYP-D3BJ/6-31G(d) level, and frequency calculation followed to ensure minimum was located. The DOS is obtained by Gaussian

broadening of the orbital level with the half width of 0.5 eV, by the Multiwfn program.
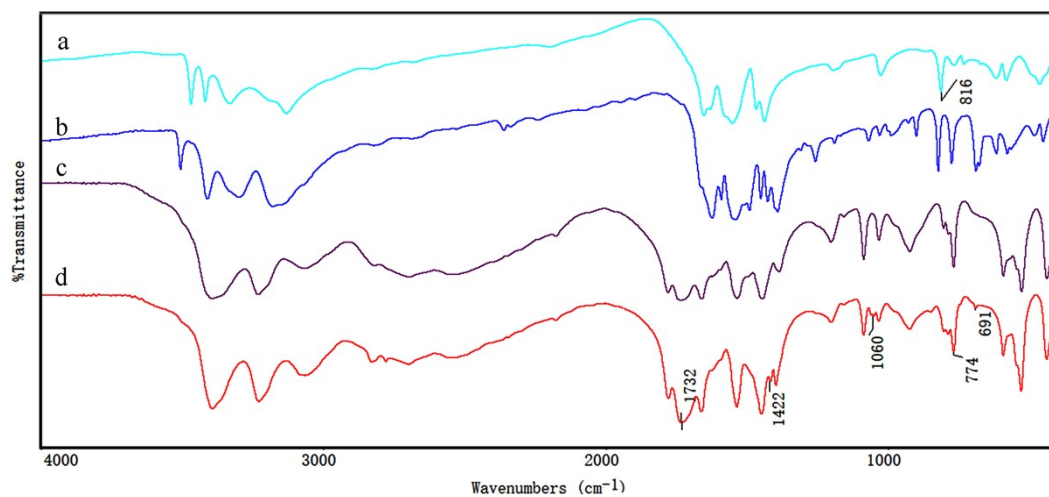
Results section

Fig. S1. FTIR spectra of (a) melamine, (b) benzonquanmine, supramolecular self-assembly of (c) melamine-cyanuric acid, and (d) melamine + benzonquanmine-cyanuric acid.
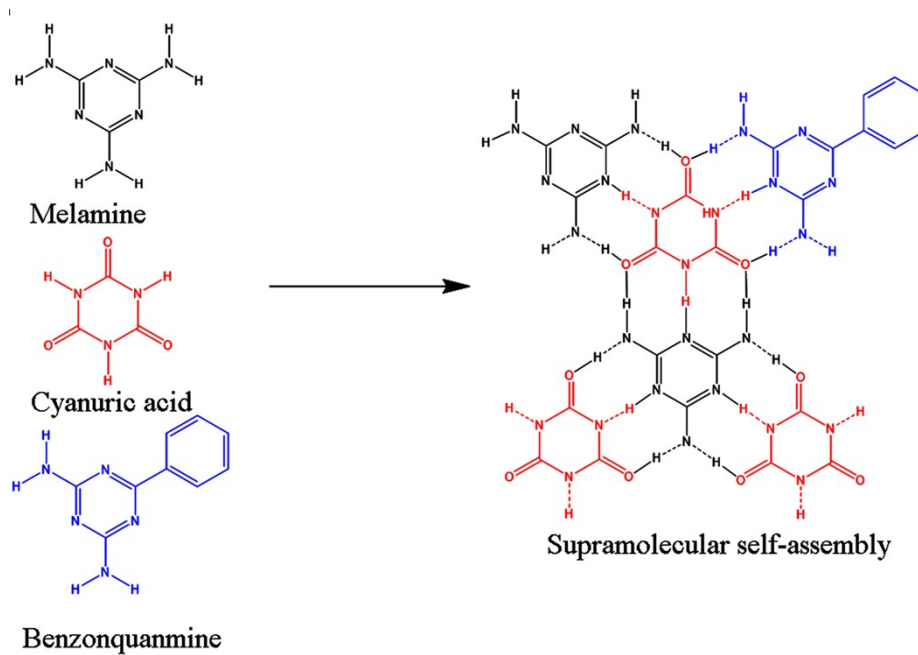

Fig. S2. Schematic illustration of the formed supramolecular self-assembly by hydrogen bonds.
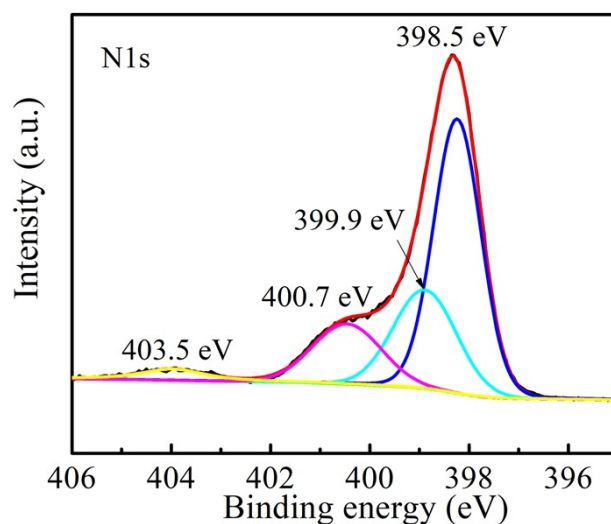
Fig. S3. The high-resolution N 1s XPS spectrum of EY-PhCN.

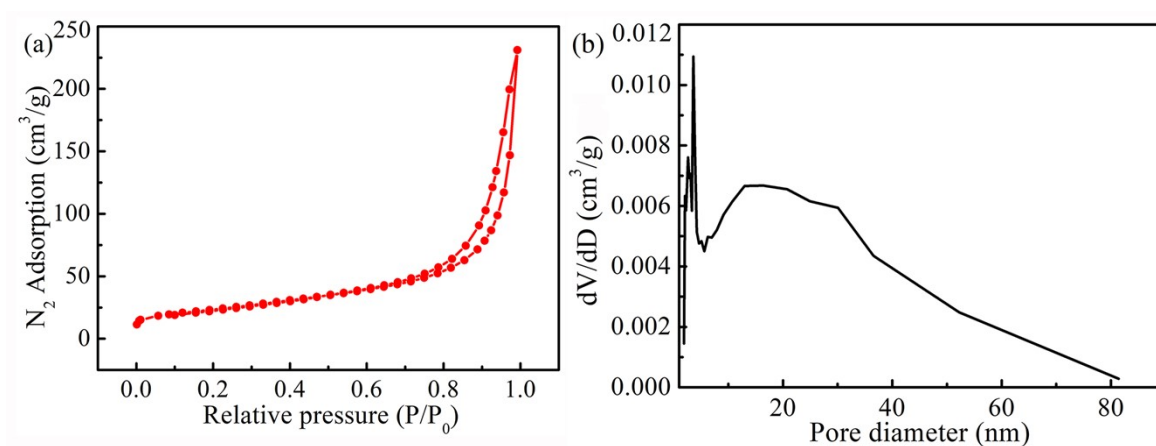The peaks at 403.5 eV can be attributed to the π excitations.

Fig. S4. (a) N_2 adsorption-desorption isotherms for the EY-PhCN and (b) pore size

distribution.

According to the pore size distribution curve of EY-PhCN, some micropore and

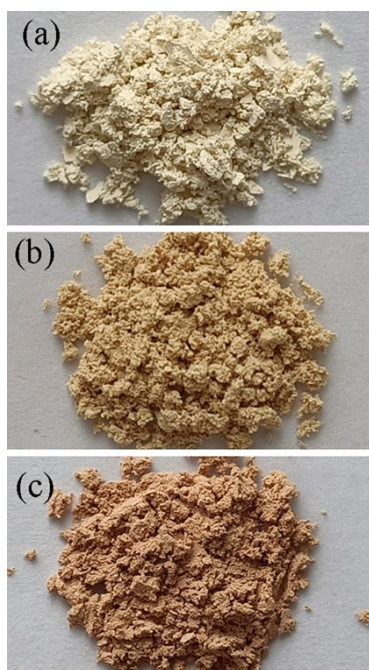mesopore were presented on its nanosheets.

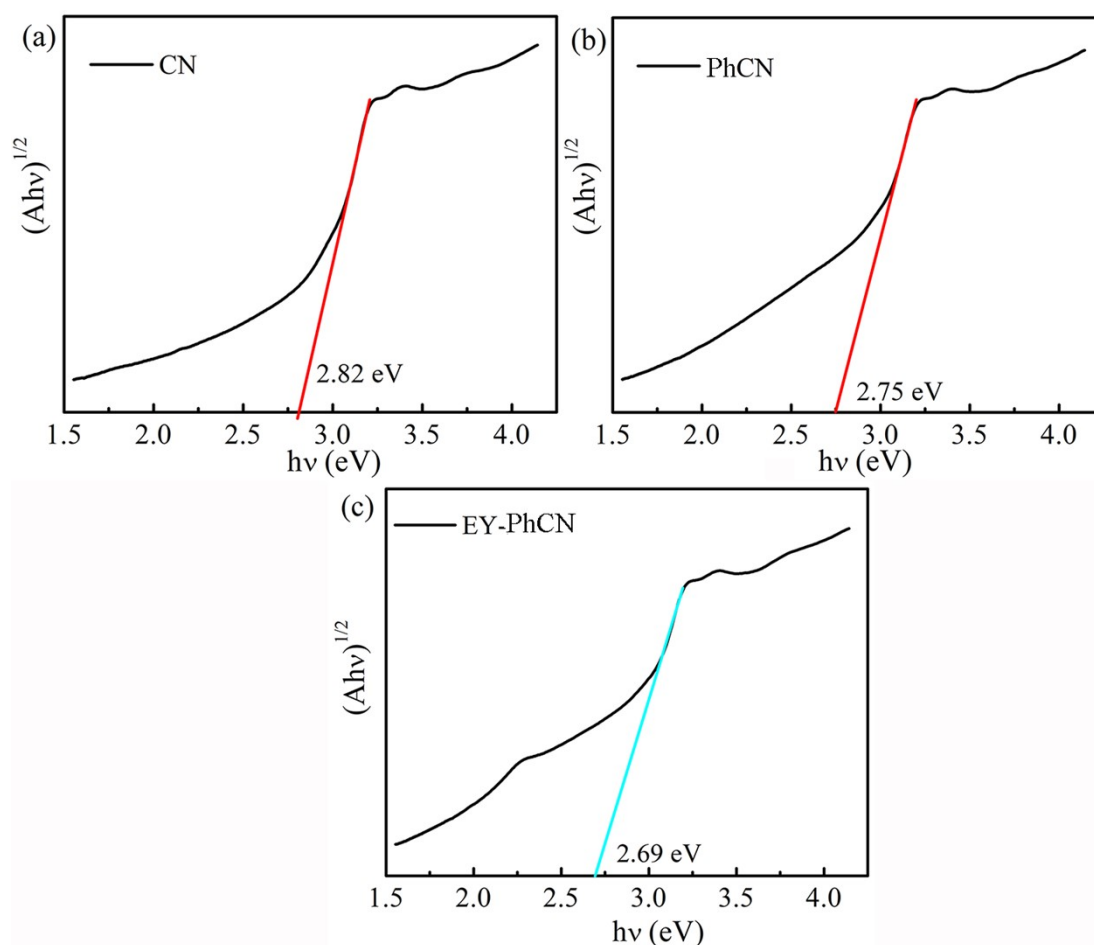**Fig. S5.** The photographs of (a) CN, (b) PhCN, and (c) EY-PhCN.

Fig. S6. $(\alpha h\nu)^{1/2}$ vs radiation energy ($h\nu$) plots of CN, PhCN, and EY-PhCN samples.
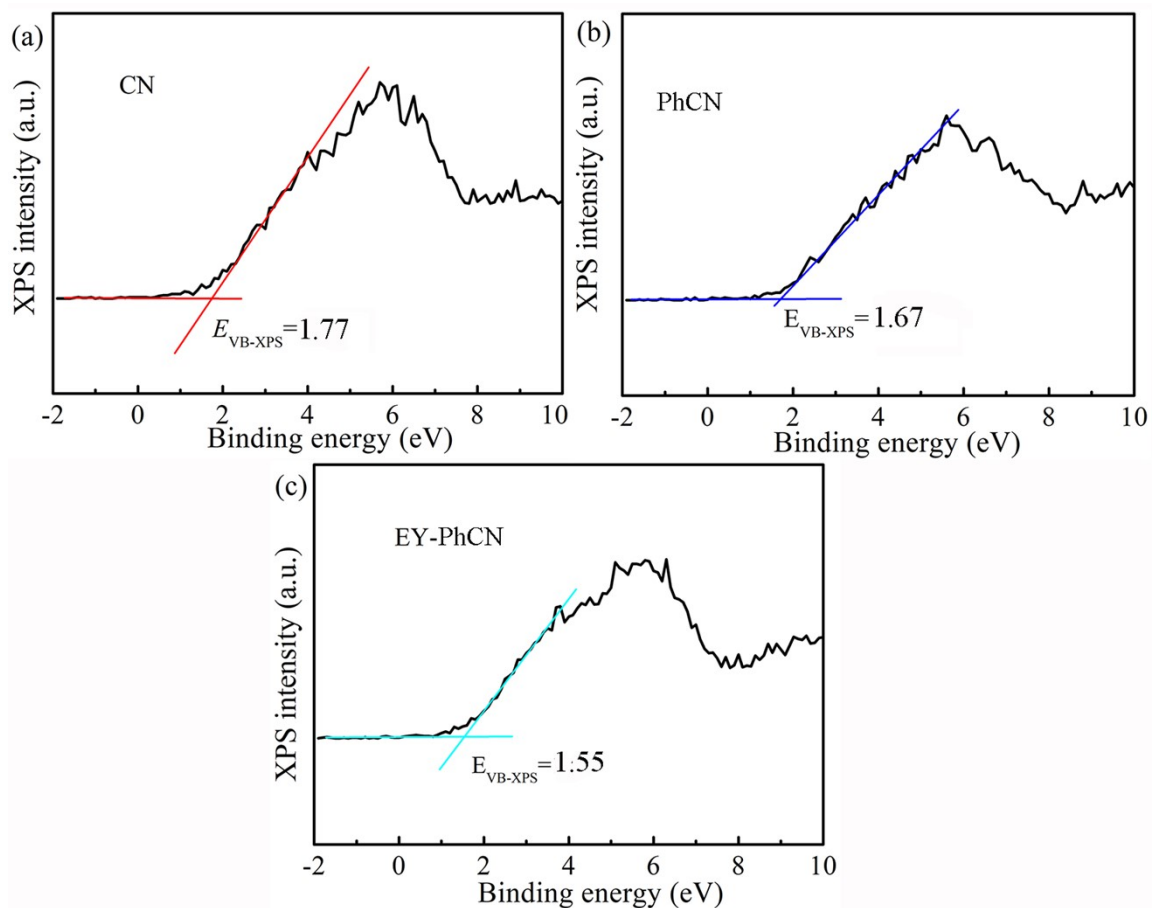
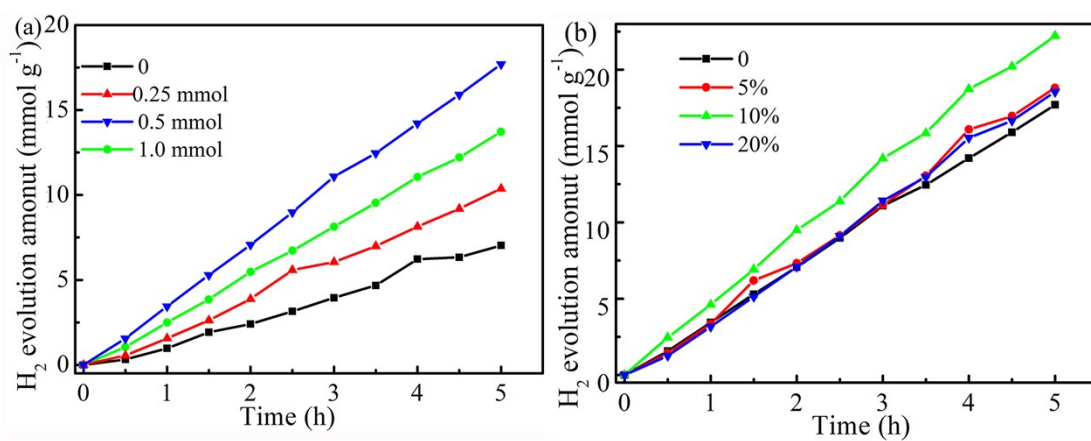**Fig. S7.** XPS valence band spectra of CN, PhCN, and EY-PhCN samples.

Fig. S8. Effect of (a) benzonquanmine and (b) EY amount on H_2 evolution activity of
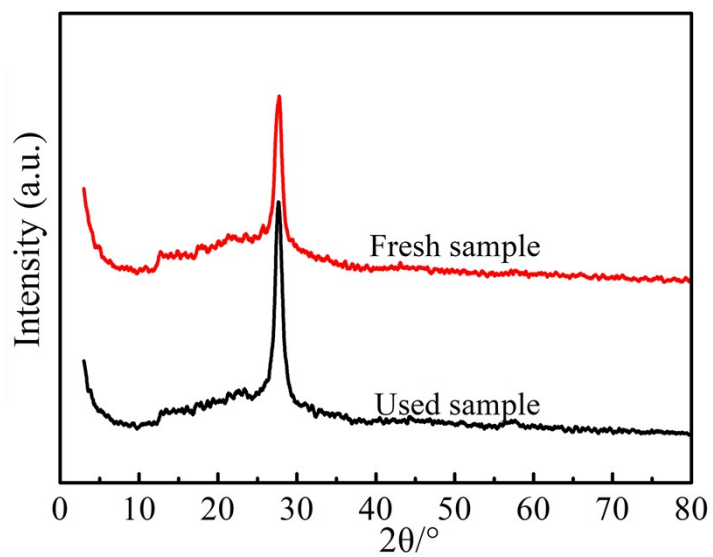
PhCN.

Fig. S9. XRD patterns of fresh and used EY-PhCN samples.
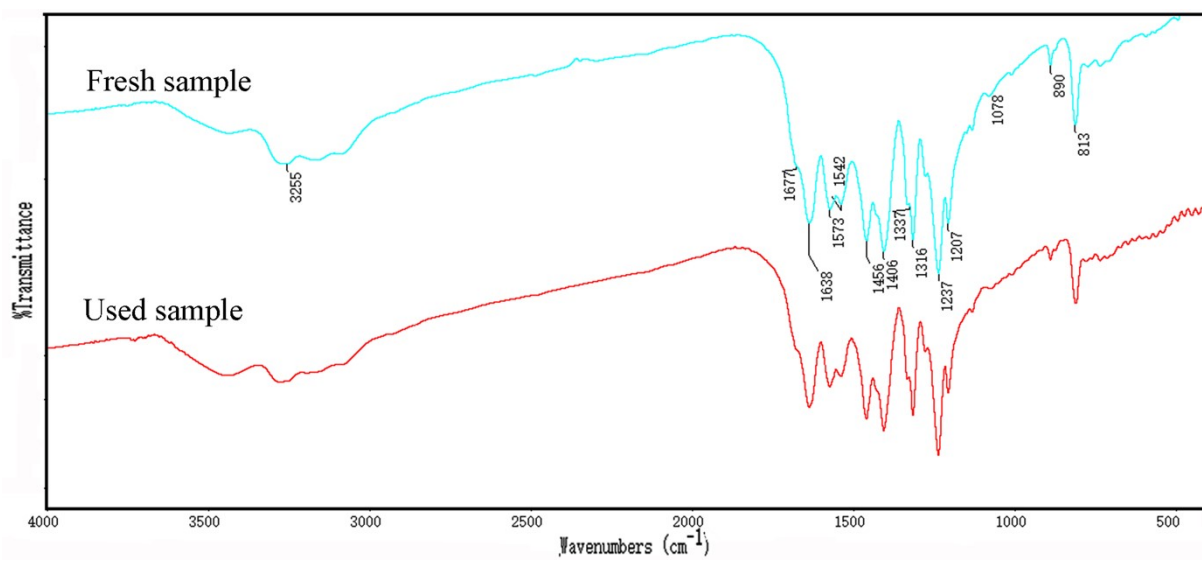

Fig. S10. IR spectra of fresh and used EY-PhCN samples.
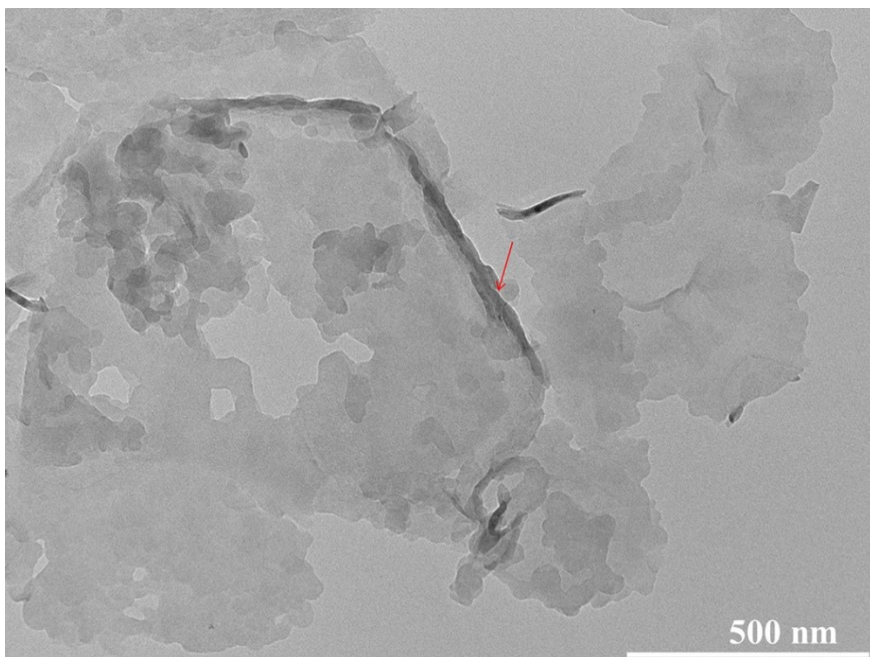
Fig. S11. TEM image of used EY-PhCN sample.
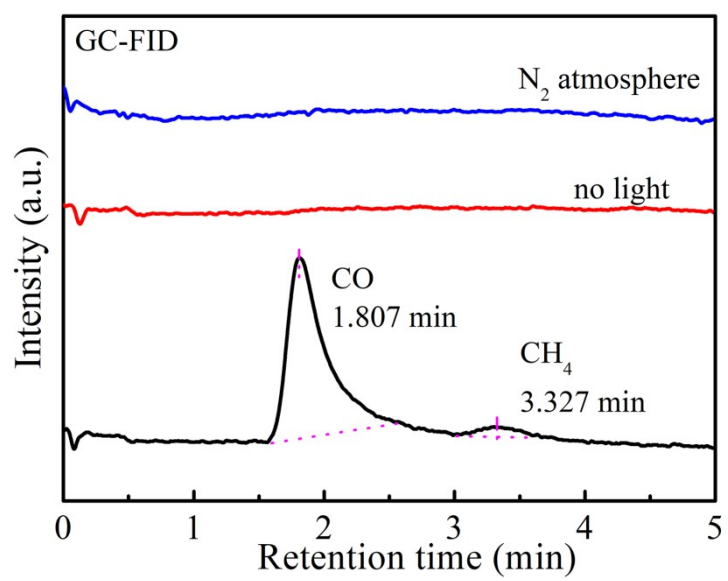
Fig. S12. The baselines of CO_2 reduction under various conditions.
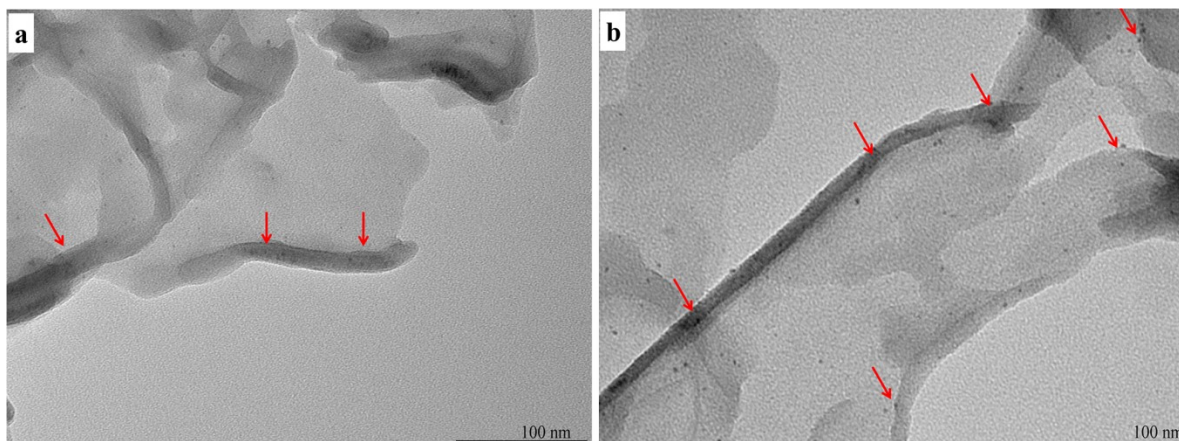
Fig. S13. TEM images of Pt-loaded EY-PhCN.
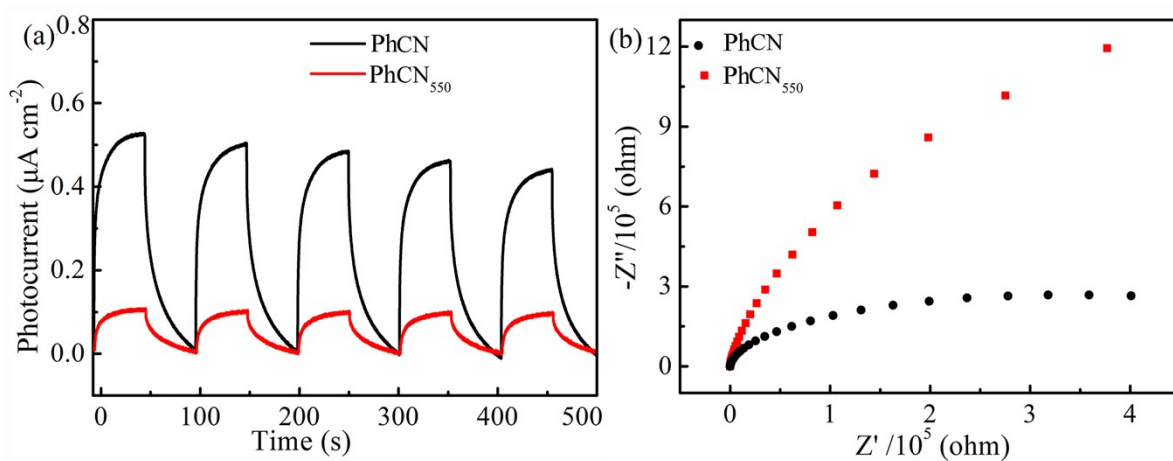
Fig. S14. (a) Transient photocurrent and (b) EIS curves of PhCN and PhCN$_{500}$.

Table S1 Proportion of each peak in the C 1s and N 1s spectra of CN, PhCN, and EY-PhCN samples.

XPS fitting peaks	CN	PhCN	EY-PhCN
	Proportion (%)		
C–C/C=C (284.6)	8.37	16.61	28.51
C–NH$_x$ (285.8)	2.06	3.36	4.93
N=C–N (288.0)	89.57	80.03	59.62
C−N=C (398.5)	68.77	54.06	50.79
N–(C)$_3$ (399.0)	16.54	28.63	24.04
C–N–H (400.5)	14.69	17.32	19.1

Table S2. The C, H, and N contents in CN-N and Ni/S-CN-N obtained by elemental analysis.

Samples	Content/%		
	C	H	N
CN	33.17	1.232	56.81
PhCN	32.83	1.305	56.17
EY-PhCN	33.09	1.347	55.27

Table S3. Comparison of photocatalytic H_2 evolution rates of various modified g-C_3N_4 photocatalysts.

Photocatalysts	r_{H_2} (μmol g^{-1} h^{-1})	photocatalyst (mg)	Reaction conditions	Light source (nm)	AQY	References
BP/g-C_3N_4	384.17	10	10% TEOA	$\lambda > 420$		1
O-CN	4210	25	1% Pt 10% TEOA	$\lambda > 420$	15.7%	2
g-C_3N_4-acetone	29330	10	2% Pt 10% TEOA	$\lambda > 420$	26.2%	3
m-CN-0.067	2500	10	0.5% Pt 15% TEOA	$\lambda > 420$		4
Mn$_{1.5}$–C_3N_4	695.1	20	0.9% Pt 10%TEOA	AM1.5	4.0%	5
C_3N_4-T-CO_2	424.7	5	3% Pt 20% TEOA	$\lambda \geq 420$	2.2%	6
CCN-1	529	100	3t% Pt 10% TEOA	$\lambda > 420$		7
CCTs	3538.3	50	3% Pt 25% methanol	$\lambda > 420$	10.9%	8
2AP-CN-15	6317.5	20	3% Pt 20%TEOA	$\lambda > 420$	20.1%	9
Pt SAs/C_3N_4	11532	50	0.91% Pt 20 % TEOA	AM 1.5G		10
SA-Cu-TCN	10600	20	1% Pt 15% methanol	$\lambda > 420$	9.2%	11
CRed-AT-C_3N_4	12310	20	3% Pt 10% TEOA	$\lambda > 420$	18.5%	12
UCN-BI400 D-A	5442.74	50	3% Pt 20% TEOA	$\lambda > 420$	23.3%	13
0.8 wt% ABT-	3638	20	2% Pt	$\lambda \geq 420$	0.64%	14

C$_3$N$_4$			10% TEOA			
Nic-CN	6310	20	1% Pt 10% methanol	λ > 420	6.81%	15
Ar-C$_3$N$_4$	10769	50	3% Pt 10% TEOA	λ > 420	10.3%	16
g-C$_3$N$_4$-MF$_{100}$ D-A	3612.65	50	3% Pt 20% TEOA	λ > 420	8.6%	17
EY-PhCN	**4443**	**10**	**1% Pt 10% TEOA**	**λ > 420**	**27.38%**	**this work**

References

[1] Q.Z. Zhang, S.Y. Huang, J.J. Deng, D.T. Gangadharan, F. Yang, Z.H. Xu, G. Giorgi, M. Palummo, M. Chaker and D.L. Ma, Ice-assisted synthesis of black phosphorus nanosheets as a metal-free photocatalyst: 2D/2D heterostructure for broadband H$_2$ evolution, *Adv. Funct. Mater.*, 2019, **29**, 1902486–1902496.

[2] J.Y. Bai, L.J. Wang, Y.J. Zhang, C.F. Wen, X.L. Wang and H.G. Yang, Carboxyl functionalized graphite carbon nitride for remarkably enhanced photocatalytic hydrogen evolution, *Appl. Catal. B: Environ.*, 2020, **266,** 118590–118598.

[3] L.S. Jiang, J. Li, K. Wang, G.K. Zhang, Y. Li and X.Y. Wu, Low boiling point solvent mediated strategy to synthesize functionalized monolayer carbon nitride for superior photocatalytic hydrogen evolution, *Appl. Catal. B: Environ.*, 2020, **260**, 118181–118190.

[4] J. Li, D.D. Wu, J. Iocozzia, H.W. Du, X.Q. Liu, Y.P. Yuan, W. Zhou, Z. Li, Z.M. Xue and Z.Q. Lin, Achieving efficient incorporation of π-electrons into graphitic carbon nitride for markedly improved hydrogen generation, *Angew. Chem. Int. Ed.*,

2019, **58**, 1985–1989.

[5] S.C. Sun, G.Q. Shen, J.W. Jiang, W.B. Mi, X.L. Liu, L. Pan, X.W. Zhang and J.J. Zou, Boosting oxygen evolution kinetics by Mn–N–C motifs with tunable spin state for highly efficient solar-driven water splitting, *Adv. Energy Mater.*, 2019, **9**, 1901505–1901513.

[6] J. Xu, M. Fujitsuka, S. Kim, Z.P. Wang and T. Majima, Unprecedented effect of CO_2 calcination atmosphere on photocatalytic H_2 production activity from water using g-C_3N_4 synthesized from triazole polymerization, *Appl. Catal. B: Environ.*, 2019, **241**, 141–148.

[7] H.L. Li, F.P. Li, Z.Y. Wang, Y.C. Jiao, Y.Y. Liu, P. Wang, X.Y. Zhang, X.Y. Qin, Y. Dai and B.B. Huang, Fabrication of carbon bridged g-C_3N_4 through supramolecular self-assembly for enhanced photocatalytic hydrogen evolution, *Appl. Catal. B: Environ.*, 2018, **229**, 114–120.

[8] Y. Wang, X.Q. Liu, J. Liu, B. Han, X.Q. Hu, F. Yang, Z.W. Xu, Y.C. Li, S.R. Jia, Z. Li and Y.L. Zhao, Carbon quantum dot implanted graphite carbon nitride nanotubes: excellent charge separation and enhanced photocatalytic hydrogen evolution, *Angew. Chem. Int. Ed.*, 2018, **57**, 5765–5771.

[9] C.M. Li, H.H. Wu, D.Q. Zhu, T.X. Zhou, M. Yan, G. Chen, J.X. Sun, G. Dai, F. Ge and H.J. Dong, High-efficient charge separation driven directionally by pyridine rings grafted on carbon nitride edge for boosting photocatalytic hydrogen evolution, *Appl. Catal. B: Environ.*, 2021, **297**, 120433–120533.

[10] Y.D. Hu, Y.T. Qu, Y.S. Zhou, Z.Y. Wang, H.J. Wang, B. Yang, Z.Q. Yu and Y.E.

Wu, Single Pt atom-anchored C_3N_4: a bridging Pt–N bond boosted electron transfer for highly efficient photocatalytic H_2 generation, *Chem. Eng. J.*, 2021, **412**, 128749–128758.

[11] X.D. Xiao, Y.T. Gao, L.P. Zhang, J.C. Zhang, Q. Zhang, Q. Li, H.L. Bao, J. Zhou, S. Miao, N. Chen, J.Q. Wang, B.J. Jiang, C.G. Tian and H.G. Fu, A promoted charge separation/transfer system from Cu single atoms and C_3N_4 layers for efficient photocatalysis, *Adv. Mater.*, 2020, **32**, 2003082–2003090.

[12] Y.L. Li, X.F. Xu, J.S. Wang, W. Luo, Z.P. Zhang, X. Cheng, J.S. Wu, Y.L. Yang, G. Chen, S.R. Sun and L.Z. Wang, Post-redox engineering electron configurations of atomic thick C_3N_4 nanosheets for enhanced photocatalytic hydrogen evolution, *Appl. Catal. B: Environ.*, 2020, **270**, 118855–118865.

[13] H.N. Che, C.M. Li, C.X. Li, C.B. Liu, H.J. Dong and X.H. Song, Benzoyl isothiocyanate as a precursor to design of ultrathin and high-crystalline g-C_3N_4-based donor–acceptor conjugated copolymers for superior photocatalytic H_2 production, *Chem. Eng. J.*, 2021, **410**, 127791–127803.

[14] C.L. Zhu, T. Wei, Y. Wei, L. Wang, M. Lu, Y.P. Yuan, L.S. Yi and L. Huang, Unravelling intramolecular charge transfer in donor–acceptor structured g-C_3N_4 for superior photocatalytic hydrogen evolution, *J. Mater. Chem. A*, 2021, **9**, 1207–1212.

[15] Q. Li, L.M. Zhang, J.N. Liu, J. Zhou, Y.Q. Jiao, X.D. Xiao, C. Zhao, Y. Zhou, S. Ye, B.J. Jiang and J. Liu, Porous carbon nitride thin strip: precise carbon doping regulating delocalized π-electron induces elevated photocatalytic hydrogen

evolution, *Small*, 2021, **17**, 2006622–2006631.

[16] W. Luo, Y.L. Li, J.S. Wang, J.C. Liu, N. Zhang, M.D. Zhao, J.S. Wu, W.Y. Zhou and L.Z. Wang, Asymmetric structure engineering of polymeric carbon nitride for visible-light-driven reduction reactions, *Nano Energy*, 2021, **87**, 106168–106178.

[17] H.N. Che, C.B. Liu, G.B. Che, G.F. Liao, H.J. Dong, C.X. Li, N. Song and C.M. Li, Facile construction of porous intramolecular g-C_3N_4-based donor-acceptor conjugated copolymers as highly efficient photocatalysts for superior H_2 evolution, *Nano Energy*, 2020, **67**, 104273–104283.